Available online at www.sciencedirect.com
ScienceDirect
European Journal of Pharmaceutics and Biopharmaceutics 65 (2007) 57–67
European Journal of Pharmaceutics and Biopharmaceutics
www.elsevier.com/locate/ejpb

Research paper

Novel ultra-rapid freezing particle engineering process for enhancement of dissolution rates of poorly water-soluble drugs

Kirk A. Overhoff [a], Josh D. Engstrom [b], Bo Chen [c], Brian D. Scherzer [d], Thomas E. Milner [c], Keith P. Johnston [b,*], Robert O. Williams III [a,*]

[a] College of Pharmacy, University of Texas at Austin, Austin, USA
[b] Department of Chemical Engineering, University of Texas at Austin, Austin, USA
[c] Department of Biomedical Engineering, University of Texas at Austin, Austin, USA
[d] The Dow Chemical Company, Midland, USA

Received 3 May 2006; accepted in revised form 19 July 2006
Available online 26 July 2006

Abstract

An ultra-rapid freezing (URF) technology has been developed to produce high surface area powders composed of solid solutions of an active pharmaceutical ingredient (API) and a polymer stabilizer. A solution of API and polymer excipient(s) is spread on a cold solid surface to form a thin film that freezes in 50 ms to 1 s. This study provides an understanding of how the solvent's physical properties and the thin film geometry influence the freezing rate and consequently the final physico-chemical properties of URF-processed powders. Theoretical calculations of heat transfer rates are shown to be in agreement with infrared images with 10 ms resolution. Danazol (DAN)/polyvinylpyrrolidone (PVP) powders, produced from both acetonitrile (ACN) and *tert*-butanol (T-BUT) as the solvent, were amorphous with high surface areas (~28–30 m^2/g) and enhanced dissolution rates. However, differences in surface morphology were observed and attributed to the cooling rate (film thickness) as predicted by the model. Relative to spray-freezing processes that use liquid nitrogen, URF also offers fast heat transfer rates as a result of the intimate contact between the solution and cold solid surface, but without the complexity of cryogen evaporation (Leidenfrost effect). The ability to produce amorphous high surface area powders with submicron primary particles with a simple ultra-rapid freezing process is of practical interest in particle engineering to increase dissolution rates, and ultimately bioavailability.

Keywords: Nanotechnology; Amorphous; Dissolution; Surface morphology; Nanoparticles; Heat transfer; Mathematical model; Ultra-rapid freezing

1. Introduction

A significant number of active pharmaceutical ingredients (APIs) being discovered display desirable therapeutic properties, but have undesirable physico-chemical properties (e.g., solubility) making formulation into an effective drug product challenging. The Biopharmaceutical Classification System (BCS) class II APIs, which have been reported to account for as many as 40% of new chemical entities [1], present particular challenges in creating successful drug products. For example, BCS class II compounds do not readily dissolve in the biological media of the digestive tract and thus exhibit poor or variable bioavailability. Consequently, the major obstacle in formulating these compounds into successful commercialized products is the difficulty in enhancing the dissolution rate.

A number of strategies and processes have been reported to facilitate the dissolution of these poorly water-soluble APIs. These include particle reduction/milling, solution-based precipitation techniques, emulsification/precipitation,

* Corresponding authors. Department of Chemical Engineering, University of Texas at Austin, Austin, USA. Tel.: +1 512 471 4617; fax: +1 512 475 7824 (K.P. Johnston); College of Pharmacy, University of Texas at Austin, Austin, TX 78712-1074, USA. Tel.: +1 512 471 4681; fax: +1 512 471 7474 (R.O. Williams III).
E-mail addresses: kpj@che.utexas.edu (K.P. Johnston), williro@mail.utexas.edu (R.O. Williams III).

0939-6411/$ - see front matter © 2006 Elsevier B.V. All rights reserved.
doi:10.1016/j.ejpb.2006.07.012

etc., as described extensively in reviews [2–6]. Cryogenic technologies, in particular, have been shown to enhance the dissolution rates of poorly water-soluble APIs by creating highly porous nano-structured particles [7–10]. The processes spray freezing into liquid (SFL) and spray freeze drying (SFD) use cryogens, particularly N_2, to form a solid dispersion or solid solution [11] composed of nanoparticle domains of API within a polymer matrix. The particles are produced by rapidly freezing a feed solution in a cryogenic liquid and removing the solvent(s) through lyophilization. Micronized powders containing nanoparticles of API have been successfully manufactured with the SFL technology using a variety of different types of solvents [12,13]. Early work utilized aqueous co-solvent systems such as tetrahydrofuran (THF)–water which has the ability to dissolve both a poorly water-soluble API as well as hydrophilic excipients. Subsequently, organic solvents such as acetonitrile (ACN) which have the unique ability to dissolve both an API and a hydrophilic excipient were used to increase API loading and reduce the risk of liquid–liquid phase separation. However, Hu et al. [14] found that increasing API loading has a profound effect on the surface morphology of the processed powders. Later, Rogers et al. [13] developed an oil-in-water (o/w) emulsion system in which the API and emulsifiers were dissolved in dichloromethane while hydrophilic stabilizers were dissolved in the aqueous phase. High-pressure homogenization was used to reduce the mean diameter of the oil droplets to less than 1 μm before freezing the sample via the SFL process.

Ultra-rapid freezing (URF) was recently developed as a particle engineering technology designed to enhance the dissolution rates and bioavailability of poorly water-soluble APIs [15]. Briefly, the process involves freezing an API contained in a polymer solution onto the surface of a cryogenic substrate with a thermal conductivity k between 10 and 20 W/(m K), collecting the frozen particles and removing the solvent. Because of rapid conductive heat transfer, resulting in high supersaturation and nucleation rates, the URF technology has the potential to create powders with superior physico-chemical properties, similar to those produced by other rapid freezing technologies. As in other freezing technologies, the rapid freezing of the API/polymer composition is critical in preventing phase separation during freezing, allowing for the active to be molecularly dispersed with the polymer. Recrystallization of the active is avoided by the inclusion of high glass-transition temperature (T_g) polymers such as polyvinylpyrrolidone (PVP) or hypromellose (HPMC).

Previously, criteria for selection of the solvent(s) suitable for the SFL process included sufficient solubility of the solids and the ability to remove the solvent without recrystallizing the API. These solvents generally have freezing points between 208 and 273 K which are ideal for tray lyophilization. Solvents with freezing points below 208 K melt during lyophilization while solvents with freezing points higher than 273 K may freeze prematurely within the atomizing nozzle. Because the URF technology applies the droplets directly onto the cryogenic substrate, premature freezing is not a concern and high freezing point solvents may be used. These solvents could prove beneficial by reducing the lyophilization time [16] or eliminating the solvent removal process altogether as some of these solvents sublime at ambient conditions or higher [17].

The objectives of this study are to introduce the URF technology as a novel method to manufacture pharmaceutical powders and to investigate how solvent properties and thin film geometry of the droplet affect the freezing rate and thus the physico-chemical properties of the final micronized powders. To determine the effect of the solvent properties, powders were manufactured from solutions from two solvents, *tert*-butanol (T-BUT) and ACN. T-BUT was selected for its higher freezing point and good lyophilization characteristics while ACN was selected for its good heat transfer properties. Heat transfer calculations of freezing rates are compared with those measured by infrared imaging. The model and results from imaging with a focal plane array infrared camera are complementary and are utilized to demonstrate differences in freezing rates between the two solvent systems. The physico-chemical properties of the processed powders were compared to those of the unprocessed bulk API, and co-ground physical mixtures to assess the potential benefit of the URF technology. The powders were evaluated based on degree of crystallinity, surface area, surface morphologies, wettability and dissolution rate. It is hypothesized that the URF technology can produce powders with enhanced physico-chemical properties, for example, low crystallinity and high surface area, leading to faster dissolution rates which could potentially enhance in vivo absorption for the BCS class II compounds.

2. Materials and methods

2.1. Materials

Micronized danazol (DAN), sodium lauryl sulfate (SLS), and polyvinylpyrrolidone (PVP) K-15 were purchased from Spectrum Chemicals (Gardena, CA, USA). High-performance liquid chromatography (HPLC)-grade acetonitrile (ACN) was obtained from EM Science (Gibbstown, NJ, USA), and *tert*-butanol (T-BUT) was purchased from Fisher Scientific (Fair Lawn, NJ, USA).

2.2. Preparation of the URF micronized powders

The compositions were prepared by dissolving DAN and PVP K15 at a 1:2 ratio and 0.55% total solids in either T-BUT heated to 313 K or ACN at room temperature. The DAN/PVP feed solutions were processed using the URF apparatus (process schematic shown in Fig. 1). The feed solutions were applied to a cryogenic solid substrate cooled to a temperature range of 193–243 K, collected, and lyophilized using a VirTis Advantage benchtop tray lyophilizer (The VirTis Company, Inc., Gardiner, NY, USA).

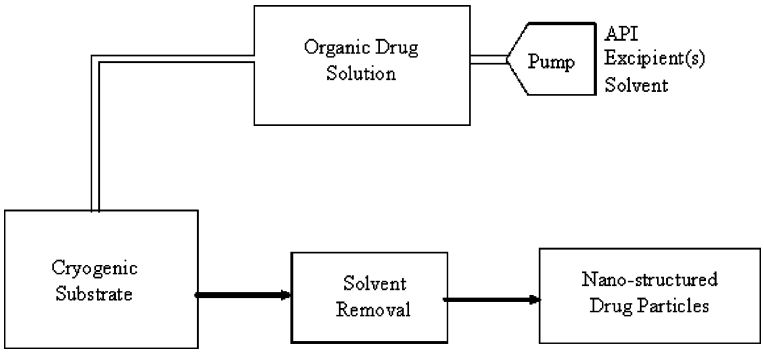

Fig. 1. Schematic of URF process.

2.3. Preparation of control powders

The bulk API was used as received while the co-ground physical mixtures were prepared by adding the API and excipients to a glass mortar and pestle and mixed/triturated using the geometric dilution technique until a uniform powder was achieved.

2.4. Infrared imaging of freezing droplets

A single droplet of ACN or T-BUT was released from a pipette with a 2 mm diameter tip 10 cm above a cryogenically cooled surface and allowed to impinge on the surface of the cryogenic substrate. An InSb focal plane array (FPA) camera (Phoenix digital acquisition system (DAS) camera, Indigo Systems, Santa Barbara, CA, USA) was positioned to acquire infrared images from above the freezing droplet on the substrate. The FPA camera detected 3–5 μm radiation, and the images were acquired at 100 frames per second (10 ms/image). The dimensions of each frame were 256 pixels by 256 pixels (15 mm × 15 mm). The image spatial resolution was approximately 40 μm per pixel. Average intensity values were calculated using MATLAB® version 6 (20 × 20 pixel square within the center of the droplet) and plotted versus time to determine the time for the center of the droplet to reach thermal equilibrium with the substrate.

2.5. Scanning electron microscopy (SEM)

The powder samples were sputter coated using a model K575 sputter coater (Emitech Products, Inc., Houston, TX, USA) with gold–palladium for 35 s and viewed using a Hitachi S-4500 field emission scanning electron microscope (Hitachi High-Technologies Corp., Tokyo, Japan). An accelerating voltage of 5–15 kV was used to view the images. All SEMs pictured were representative of the entire sample.

2.6. Dissolution testing

Dissolution testing was performed on all powder samples using a United States Pharmacopeia (USP) 24 Type 2 apparatus (VanKel VK6010 Dissolution Tester with a Vanderkamp VK650A heater/circulator, Cary, NC, USA). The dissolution medium consisted of 0.3% SLS dissolved in de-ionized water and maintained at 37.0 ± 0.2 °C throughout the study. Five milliliter samples were withdrawn at 2, 5, 10, 20, 30 and 60 min time points, filtered using a 0.45 μm GHP Acrodisc filter and analyzed using a Shimadzu LC-10 liquid chromatograph (Shimadzu Corporation, Kyoto, Japan) equipped with an Alltech ODS-2, 5 μm C_{18} column (Alltech Associates, Inc., Deerfield, IL, USA). A 70:30 ACN–water mobile phase at 1 ml/min eluted the DAN peak at 5 min [11]. The maximum absorbance was measured at $\lambda = 288$ nm. System suitability requirements were met ($R^2 \geqslant 0.999$, precision $\leqslant 2.0\%$ RSD).

2.7. X-ray powder diffraction (XRD)

The X-ray diffraction patterns of all powder samples were analyzed using a Philips 1710 X-ray diffractometer with a copper target and nickel filter (Philips Electronic Instruments, Inc., Mahwah, NJ, USA). The leveled powder was measured from 5 to 45 2θ degrees using a step size of 0.05 2θ degrees and a dwell time of 1 s.

2.8. Surface area analysis

Specific surface area was measured using a Nova 2000 v.6.11 instrument (Quantachrome Instruments, Boynton Beach, FL, USA). A known weight of powder was added to a 12 mm Quantachrome bulb sample cell and degassed for a minimum of 3 h. The sample was then analyzed ($n = 3$) by the NOVA Enhanced Data Reduction Software v. 2.13 via the Brunauer, Emmett, and Teller theory of surface area [18].

2.9. Contact angle measurement

A 50 mg aliquot of sample powder was compacted with a Model M Carver laboratory press (Fred S. Carver, Inc., Menomonee Falls, WI, USA) using a compaction force of 500 kg to form a smooth surfaced tablet. A 3 μl drop of purified water was added to the surface of the tablet and

the contact angle was quantitated using a goniometer (Ramè-Hart Inc., Mountain Lakes, NJ, USA) by measuring the tangent to the curve of the droplet on the surface of the tablet.

2.10. Statistical analysis

One-way analysis of variance (ANOVA) was used to determine statistically significant differences between results. Results with p values <0.05 were considered statistically significant. Post hoc comparisons using Tukey's test were made to determine differences between the URF compositions and the controls.

3. Results

3.1. Infrared measurements of cooling droplets on cryogenic plate

An infrared (IR) camera was used to quantitate the amount of IR energy radiated from the spread droplet over time on a cryogenic plate. The IR camera outputs intensity values assigned on a grayscale with white having a high intensity and black having a low intensity in relation to the amount of radiant energy emitted from the droplet. A thermal equilibrium was established when the intensity value was constant over time, indicating that the rate of heat transfer approached zero. It is estimated that at thermal equilibrium, the temperature of the droplet is near the temperature of the cryogenic substrate and confirmed via direct thermocouple measurement using a surface measuring probe. As the droplets enter the field of view, they appear white for both ACN and T-BUT. Figs. 2 and 3 contain time lapse IR photographs for ACN and T-BUT, respectively. In addition, IR video for the ACN and TBUT droplets can be seen in MovieACN and MovieTBUT, respectively. The videos more clearly demonstrate the freezing process occurring for the time lapse pictures in Figs. 2 and 3. For ACN, complete spreading of the droplet occurred within the first 10 ms interval indicating that the time of droplet spreading, $t_{\text{spreading,}}$ was much less than the freezing time, t_{freeze}. Therefore, $t = 0$ was defined as the first frame in which impingement was observed. When dropped from a height of 10 cm, the diameter for the spread ACN droplet as measured by a ruler and confirmed by IR camera was 1.9 cm. At $t = 20$ ms, the droplet began to visually darken evenly throughout the entire droplet. Since IR radiation between 3 and 5 μm is not readily absorbed by either ACN or T-BUT, it is believed that the initial darkening is a result of the cooling of the solvent near the droplet–surface interface. Between 20 and 70 ms, a cooling front is observed moving radially inward as the remaining droplet freezes. After 70 ms a slight fluctuation in intensity is observed before thermal equilibrium around 2280 intensity units is established. Fig. 4a is a plot of the average intensity at the center of the ACN droplet as a function of time. After a rapid decrease in intensity is initially observed in which the bottom of the solvent

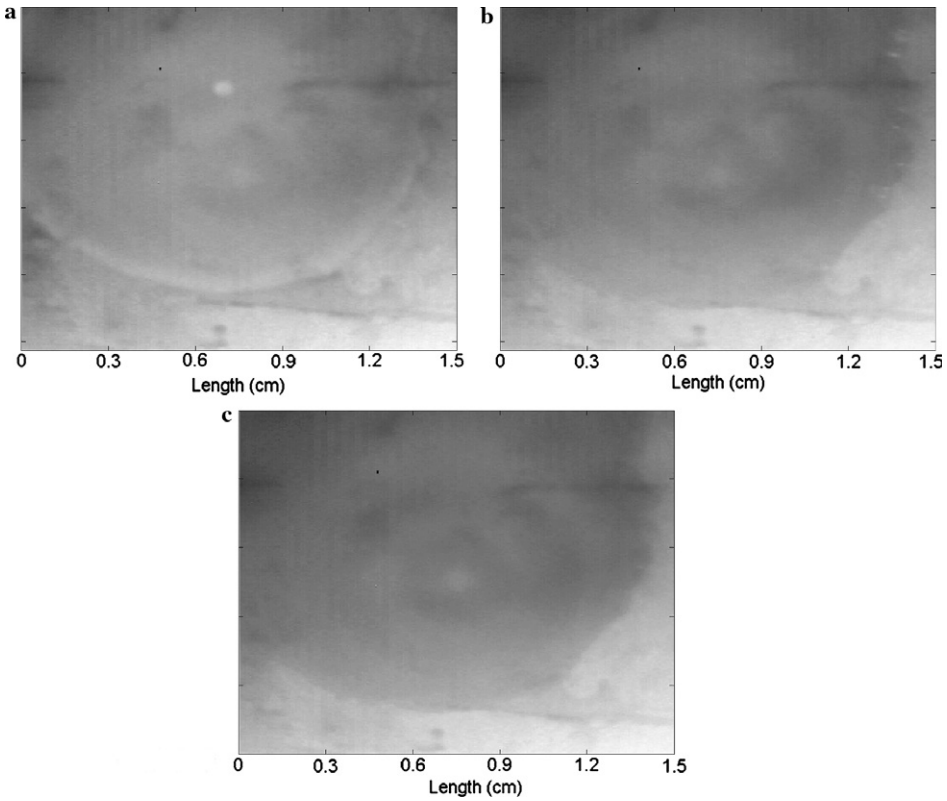

Fig. 2. IR photographs of ACN droplet impinging and freezing on −60 °C surface at $t = 0$ ms (a), $t = 20$ ms (b), and $t = 70$ ms (c).

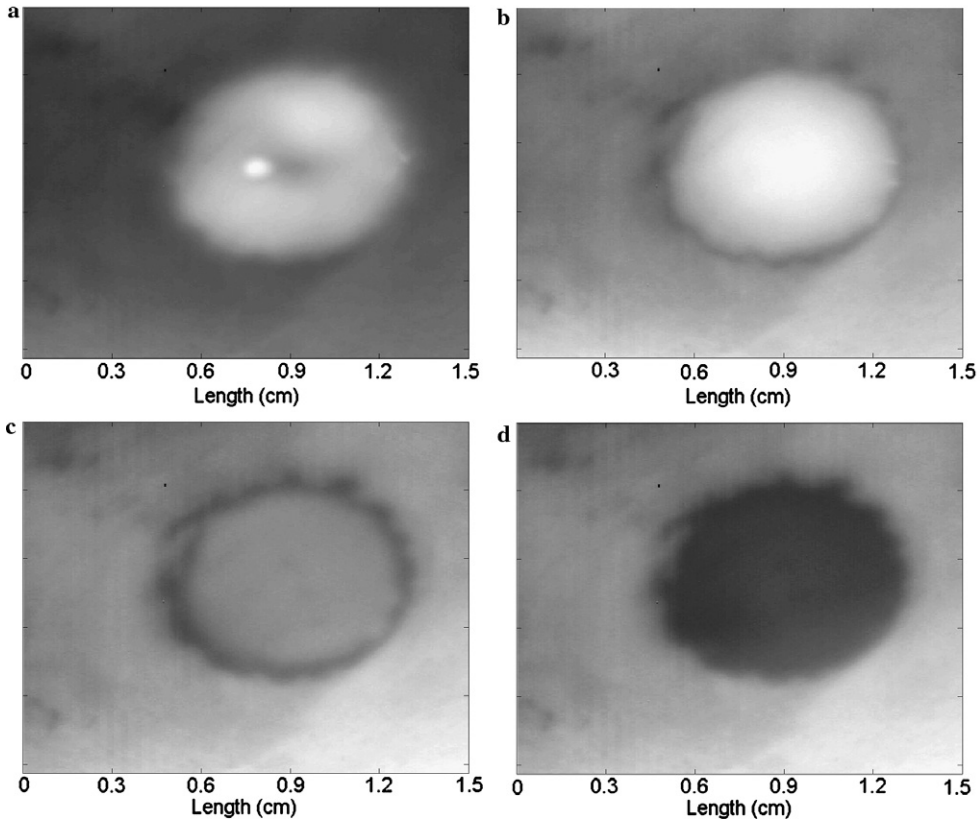

Fig. 3. IR photographs of T-BUT droplet impinging and freezing on −60 °C surface at $t = 0$ ms (a), $t = 150$ ms (b), $t = 400$ ms (c), $t = 1000$ ms (d).

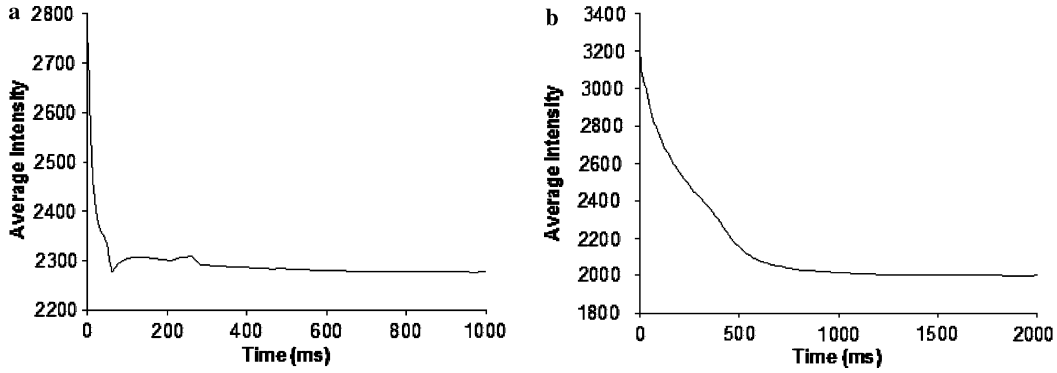

Fig. 4. IR droplet intensity versus time for ACN (a) and T-BUT (b).

immediately freezes, the rate begins to slow slightly until a minimum intensity value of 2280 is reached at 70 ms.

With a melting point near room temperature (296–298 K), the T-BUT samples were heated to 313 K to prevent premature freezing before spreading of the droplet on the cryogenic surface. As in the case of the ACN droplet, impingement and complete spreading of the T-BUT droplet also occurred within the first 10 ms interval. When dropped from a height of 10 cm, the spread diameter for the frozen T-BUT droplet measured 0.8 cm, less than half that of the ACN droplet. At 150 ms, the appearance of a black ring around the edge of the droplet appears indicating that the cooling rate is faster near the edge of the droplet (Fig. 3b). As cooling continues, the cooling front proceeds radially inward towards the center of the droplet and has much greater contrast than observed with the ACN droplet. At 400 ms, IR intensity throughout the droplet was decreased (Fig. 3c) and at 1000 ms thermal equilibrium was established (Fig. 3d). Similar to the case for the ACN droplet, the first few frames indicate a sharp decrease in intensity as the liquid in contact with the cryogenic surface immediately cools (Fig. 4b). After the initial drop in intensity where the droplet freezes instantaneously at the solid–liquid interface, the rate of intensity decrease begins to slow and becomes much slower than for the ACN droplet. Since solidification occurs in the axial direction according to this model, the resulting solid solvent and solid API/polymer particles act as an insulating layer [19] decreasing the rate of heat transfer. Ultimately, the droplet thermally equilibrates around 2030 at around 1000 ms.

3.2. Physico-chemical properties and dissolution rates of URF-processed powders

DAN powders were produced using the URF technology, and the physico-chemical properties were compared to those of the bulk API and the physical mixture. The characteristic crystalline peaks for DAN were found at 15.90 and 19.15 2θ degrees with a doublet peak around 17.30 2θ degrees, as seen in the bulk DAN and physical mixture samples in Fig. 5. The physical mixture sample showed a reduction in crystalline intensity due to the dilution of PVP in the sample. Both URF-processed powders lacked the characteristic crystalline peaks and therefore were considered to contain amorphous DAN. This is attributed to the rapid freezing occurring during the URF process and the ability of PVP to inhibit crystal growth.

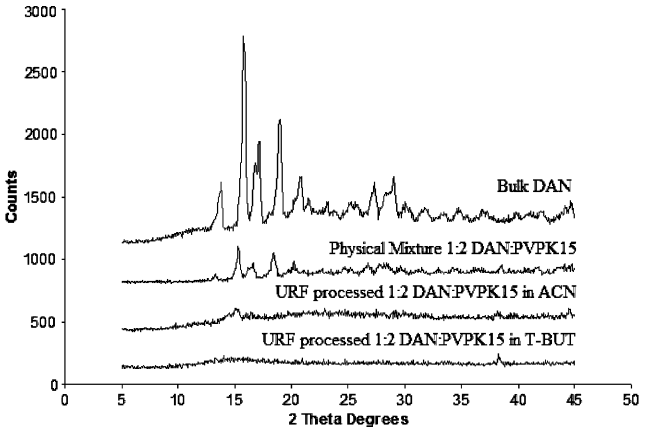

Fig. 5. X-ray diffraction patterns of processed DAN/PVP compositions compared to bulk DAN.

Table 1
Surface area and contact angles of the URF compositions investigated

Composition	Surface area (m^2/g)	Contact angle (°)
URF 1:2 DAN/PVPK15 (in ACN)	25.93	30.5 ± 0.5
URF 1:2 DAN/PVPK15 (in T-BUT)	29.33	32.5 ± 0.5
Phys. Mix. 1:2 DAN/PVPK15	0.69	39.5 ± 4.5[a,b]
Bulk DAN	0.52	64.0 ± 3.0[a,b]

Using Tukey's HSD test, $\mathrm{HSD} = q\sqrt{\frac{s^2}{N}} = 3.85$.

[a] Statistically different from URF 1:2 DAN/PVPK15 in ACN.

[b] Statistically different from URF 1:2 DAN/PVPK15 in T-BUT.

As seen in Table 1, high specific surface areas (SSAs) were reported for both the URF-processed powders from T-BUT, with values of 29.3 and 25.9 m^2/g, respectively. The SSA was 50–60× greater than that of the micronized bulk DAN and about 40× greater than that of the physical mixture.

Differences between the two URF-processed powders are evident in the surface morphology. The URF-processed powder from ACN showed compacted aggregates of uniform nanoparticles with diameters of about 100 nm or smaller (Fig. 6a) in all areas of the sample. The surface morphology of the 1:2 DAN/PVP composition dissolved in T-BUT and processed by URF indicated regions of nanoparticles with similar particle sizes (Fig. 6b); however, particle sizes were not as uniform as those present from powders produced from ACN. Likewise, other areas of the powder exhibited very thin plate-like domains.

Dissolution rates for the processed powders are compared in Fig. 7 with those of the bulk DAN and the physical mixture. Samples processed from URF revealed rapid dissolution with at least 85% API dissolved within 10 min and showed statistically greater release than the bulk DAN and the physical mixture ($p < 0.05$). The URF-processed powders produced from both T-BUT and ACN

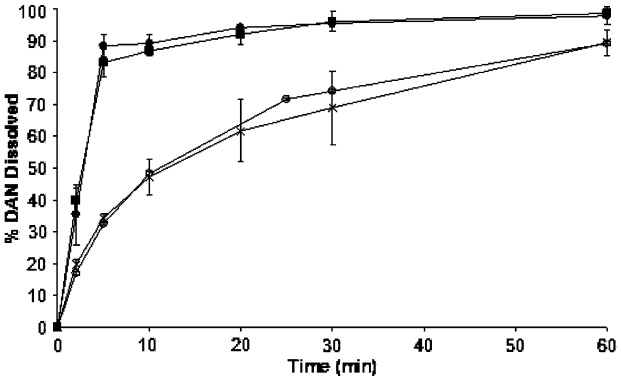

Fig. 7. Dissolution profile for URF-processed 1:2 DAN/PVPK15 in ACN (●), URF-processed 1:2 DAN/PVPK15 in T-BUT (■), 1:2 DAN/PVPK15 physical mixture (○), and bulk DAN (×).

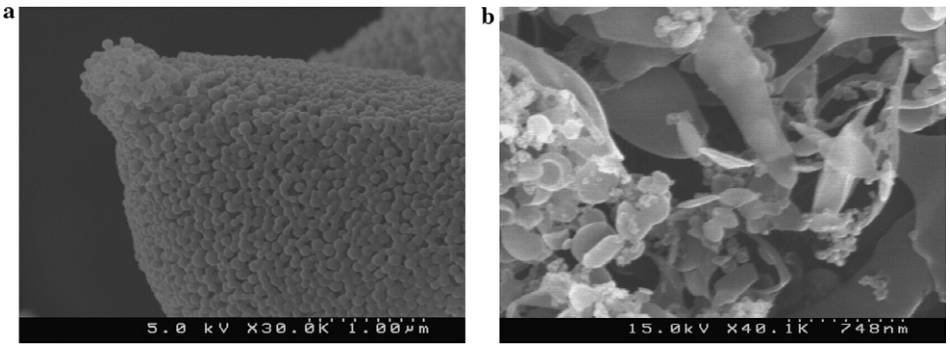

Fig. 6. SEM micrographs of URF-processed 1:2 DAN/PVPK15 in ACN (a), URF-processed 1:2 DAN/PVPK15 in T-BUT (b).

had nearly identical dissolution profiles ($p > 0.05$). The similar profiles may be rationalized by the observation that both compositions were amorphous and had similar and very high surface areas. These factors produced very rapid dissolution rates. Inclusion of PVP in the physical mixture increased the dissolution only slightly, relative to pure danazol indicating that the low surface area and crystallinity of DAN limited the dissolution rate.

ANOVA statistical analysis revealed that significant differences in contact angle existed between the four sample groups ($F > F_{crit}$). Contact angle measurements for both the processed powders and the physical mixture of 1:2 DAN/PVPK15 showed a statistically significant ($p < 0.05$) decrease in contact angle (30.5–39.5°) compared to the bulk DAN (64.0°) indicating better wettability of the powders as seen in Table 1. There were no significant differences between the two URF-processed powders (e.g., $\bar{X}_{\text{T-BUT}} - \bar{X}_{\text{ACN}} = 2.5 < 3.85$) but there were differences between the URF-processed powders and the physical mixture. This is most likely due to the intimate mixing of PVP and DAN during the process allowing for a more homogeneous distribution of the PVP throughout the powder.

4. Discussion

4.1. Theoretical modeling

The phenomena of droplet spreading and solidifying/freezing for an impinging droplet on a solid substrate have been studied extensively by many research groups [19–32]. The fluid dynamics and heat transfer can be coupled requiring a numerical solution. However, in our IR imaging studies the heat transfer was much slower than the droplet spreading. Thus, the model can be solved analytically to describe the cooling rate in URF [33]. The validity of the model will be evaluated by comparison to the experimental IR data for ACN and T-BUT.

In the model it is first assumed that droplet spreading after impact occurs on a much shorter time scale than heat transfer. Consequently, significant heat transfer does not occur until spreading is complete. The second assumption is that the droplet spreads to form a thin cylindrical disk. Because of the small height of the disk relative to the diameter, the third assumption is that only one-dimensional heat transfer is present in the z direction. Conduction in the radial direction through the thin disk parallel to the surface may be neglected. The final assumption is that the thermal diffusivity α is constant over the entire temperature range and remains unchanged during the phase change of freezing. Given the above assumptions the transient heat transfer equation through the cylindrical disk simplifies to

$$\frac{\partial T}{\partial t} = \alpha \frac{\partial^2 T}{\partial x^2}, \tag{1}$$

where the temperature T is a function of time t and x is the distance into the disk from the top surface of the thin film exposed to air. The thermal diffusivity of the spread droplet is defined as $\alpha = k/\rho * C_p$, where k is the thermal conductivity, ρ is the density, and C_p is the heat capacity.

The first boundary condition for Eq. (1) assumes that heat transfer through the top surface of the disk exposed to the air is negligible. Therefore, the air is assumed to act as an insulator. The second boundary condition assumes the cryogenic plate temperature, T_{plate}, remains constant during the cooling process with negligible heat transfer resistance between the plate and spread droplet. These boundary conditions are

$$\left.\frac{\partial T}{\partial x}\right|_{x=0} = 0, \tag{2}$$

$$T(L,t) = T_{\text{plate}}. \tag{3}$$

Here $x = L$ is the bottom surface of the disk in contact with the plate. The initial condition assumes that the droplet temperature is uniform before impact and is defined as:

$$T(x,0) = T_{\text{i}}, \tag{4}$$

where T_i is the initial solvent temperature. Eq. (1) is then solved analytically for a finite disk thickness [33] to give

$$T(x,t) = T_{\text{plate}} + \frac{2}{L}\sum_{n=0}^{\infty} e^{-\alpha(2n+1)^2\pi^2 t/4L^2} \times \cos\frac{(2n+1)\pi x}{2L}\left\{\frac{2L(-1)^{n+1}T_{\text{plate}}}{(2n+1)\pi} + \int_0^L T_i \frac{\cos(2n+1)\pi x'}{2L}\,dx'\right\}, \tag{5}$$

where L is the disk thickness. Cooling times are then determined by calculating the time, t, it takes for the surface of the solvent film at $x = 0$ with thickness L to reach a given temperature T using the software MATHCAD® version 11.

The spread droplet thickness was easily determined with the assumption that the droplet impacting on the cold substrate deformed into a cylinder with an equivalent volume to the original droplet volume before impact. Droplet volume was determined by dropping 100 droplets into a graduated cylinder and measuring the total volume. Frozen spread droplet diameters were measured with a ruler across two directions and averaged for 10 droplets. Droplet thicknesses were then calculated from the known volume of the falling droplet and the diameter of the frozen spread droplet and were 109 ± 10 and 403 ± 32 μm for ACN and T-BUT, respectively. Modeling the frozen spread droplet as a thin cylindrical disk has been used in many previous models [20–22,25,34] and has been experimentally justified when the Weber number, $We = \rho V^2 D/\gamma$ (inertial to interfacial forces), of the impacting droplet is $\gg 1$ [26] where V is the impact velocity, D is the droplet diameter, and γ is the droplet interfacial tension. The impact velocity, V, was calculated from the free-fall equation in a gravitational field, $V = (2gH)^{1/2}$ [34], where the falling height, H, of the droplet was 10 cm resulting in an impact velocity of 1.4 m/s.

The densities and interfacial tensions for each solvent were determined using the DIPPR database (Brigham Young University, Provo, UT) at the initial temperatures of 298 and 313 K for ACN and T-BUT, respectively. The resulting We numbers were 207 and 274 for the ACN and the T-BUT droplets, respectively, which supports the assumption that the impinging droplets deform into thin cylindrical disks [26]. The thermal diffusivity, α, used for each solvent in this model was determined by first taking the average of each property in the definition of α evaluated between the initial droplet temperature to the freezing temperature of each solvent (Table 2). The α for each solid solvent was not determined since thermal conductivity values were not available for each solvent in solid form.

The calculation of cooling times for each solvent was based on the time it takes for the top of the spread droplet at $x = 0$ to reach a given temperature, T. The cooling time to reach the freezing point of each solvent was calculated first. Fig. 8a is the calculated temperature profile for an ACN spread droplet. After 72 ms the top of the spread droplet defined at $x = 0$ reaches the freezing point of ACN, 230 K. For T-BUT (Fig. 8b) the cooling time to reach the freezing temperature of 299 K was 483 ms. Since the freezing points of each solvent are greater than the surface temperature of the solid substrate, 213 K, the spread droplet will continue to cool below the freezing point until an equilibrium temperature is reached. Therefore, a cooling time was calculated for the droplet to reach an arbitrary temperature of 225 K, which is approximately 5% greater than the cryogenic substrate temperature. These times were 86 and 3037 ms for ACN and T-BUT, respectively.

Table 2
Thermal and physical properties used to calculate t_{freeze} for ACN and T-BUT

Property	ACN[a]	T-BUT[b]
k (W/m K)	0.218	0.121
ρ (g/cm^3)	0.811	0.774
C_p (J/g K)	2.182	3.057
α (cm^2/s)	0.0012	0.00051
Estimated t_{freeze} (ms)	61	629
Measured t_{equil} (ms)	70	1000

[a] For ACN, the average values calculated at $T_{freeze} = 229$ K and $T_i = 298$ K.
[b] For T-BUT, the average values calculated at $T_{freeze} = 298$ K and $T_i = 313$ K.

4.2. Comparison of ACN IR data to calculated cooling times

To evaluate the accuracy of the predictions of the proposed model, the calculated cooling times were compared to the IR images. The initial intensity of 2783 for time $t = 0$ ms correlated to the initial ACN temperature of 25 °C (Fig. 4a). Due to the small thickness of the spread droplet it is reasonable to assume that the equilibrium intensity of 2280 at the top surface of the spread droplet is close to the temperature of the cryogenic substrate (213 K). The calculated cooling times to reach the freezing point, 230 K, and 225 K were 72 and 86 ms, respectively. The similarity in these times is consistent with the small difference in temperature between the freezing temperature and 225 K. The calculated cooling time is located at the bottom of the initial steep descent for the experimental curve in Fig. 4a. The calculated equilibrium cooling time occurs shortly thereafter at the beginning of the flat part of the intensity curve. The abrupt change in slope of the intensity curve near 70 ms may be an indication of ACN changing from the liquid to solid phase. The discontinuity in the slope of the intensity curve was confirmed when the experiment was repeated a second time. The good agreement between the calculated cooling times and the shape of the intensity curve supports the assumption that the heat

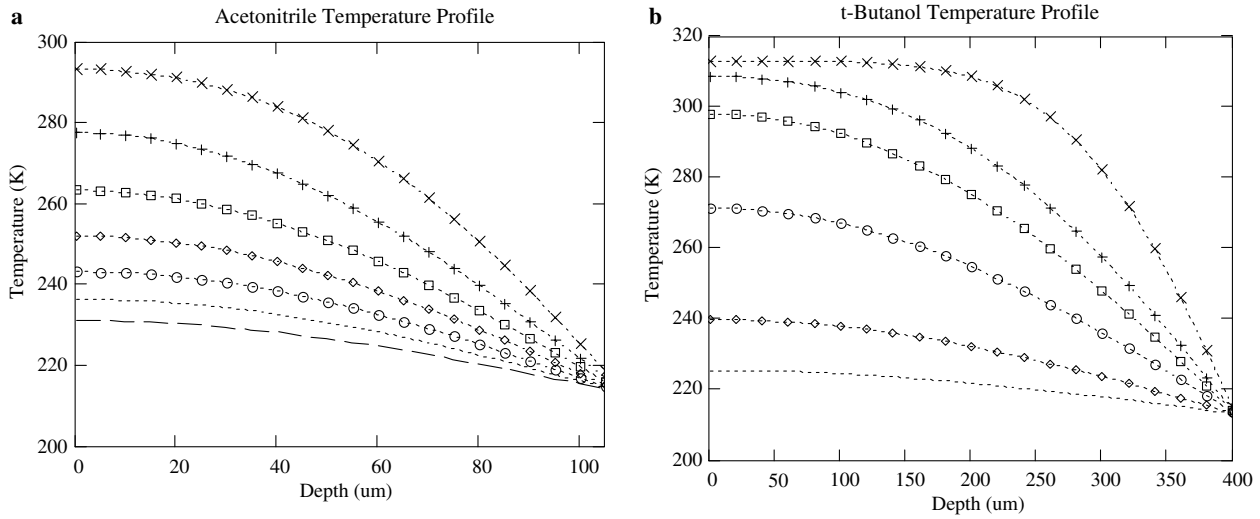

Fig. 8. Theoretical temperature profile of ACN droplet (a) on a cryogenic surface at 10 ms (×), 20 ms (+), 30 ms (□), 40 ms (◇), 50 ms (○), 60 ms (···), and 70 ms (−). Theoretical temperature profile of T-BUT droplet (b) on a cryogenic surface at 100 ms (×), 300 ms (+), 500 ms (□), 1000 ms (○), 2000 ms (◇), and 3000 ms (···).

transfer time is considerably slower, and essentially uncoupled, from the rapid spreading of the droplet on impact. Frame-by-frame analysis of the impinging ACN droplet showed that complete spreading occurred in less than 10 ms. Furthermore, the spreading diameter on the cryogenic substrate was similar to that on the same substrate at room temperature, indicating that cooling and freezing of the droplet did not inhibit spreading. Although the model calculates cooling times that are consistent with experimental IR data, it does not account for the radial cooling front observed during the latter stages of cooling of the spread ACN droplet. In spite of the radial cooling front observed during cooling, the calculated cooling times do not vary significantly from the experimental cooling times.

4.3. Comparison of T-BUT IR data to calculated cooling times

The cooling behavior was substantially different for T-BUT compared to ACN. As shown in Fig. 3, cooling along the radial direction of the spread T-BUT droplet appeared to be significant. Also, after the T-BUT droplet impacted the cryogenic substrate the final spread droplet diameter was only 0.8 cm which was significantly smaller compared to the 1.9 cm formed on the same substrate at room temperature. The smaller spread diameter corresponds to a frozen spread droplet thickness 4× greater than ACN. The calculated cooling time to freezing (299 K) for T-BUT was 483 ms starting from an initial droplet temperature of 313 K. In Fig. 4b the approximate intensity value at $t = 483$ ms was 2185 which was slightly above the asymptotic equilibrium intensity (~213 K) of 2016, but well below the initial intensity of 3227 correlated to 313 K. The intensity curve reaches equilibrium at approximately $t = 1000$ ms which is assumed to correlate to an approximate spread droplet surface temperature of 213 K. The calculated time for the top droplet surface to reach the defined equilibrium temperature of 225 K was 3037 ms which is about 3-fold the experimental value of 1000 ms. However, the model correctly predicted that the experimental observation that the cooling was much slower than for ACN.

Various factors may contribute to the faster cooling in the experiments versus the model. The difference cannot be explained by cooling of the droplet during free fall. The free-fall cooling effect on droplets, initially at 313 K, according to the model of Bennett and Poulikakos, [34], would produce an insignificant change of less than 1 K. The more rapid cooling for the experimental measurements may be the result of radial cooling as the droplet spread, and even after spreading. The movement of the radial cooling front was about 30× slower for T-BUT than for ACN. Thus, radial cooling appeared to play a greater role for T-BUT, which is consistent with the thicker disk for T-BUT, which corresponds to a greater cross-sectional surface area for radial conduction, and a smaller surface area for axial conduction.

The effect of radial cooling was shown for molten metal droplets impinging on a cold substrate by other research groups [19,32]. It was determined that significant heat transfer can occur during spreading of the droplet after impact [19,32]. Zhao et al. described that the radial cooling front occurs because during impaction high temperature solvent is continuously supplied to the center region of impact while the spreading front cools at a faster rate by contacting the low temperature surface of the substrate [32]. Fukai et al. determined that the spreading diameter of droplets can be arrested on a cold substrate as the edges freeze [19]. It is likely that the spreading diameter was reduced for T-BUT by freezing of the droplet edge, since the temperature difference from the initial droplet temperature (313 K) to freezing point (299 K) is only 14 K versus 68 K for ACN. The effect of radial cooling and partial cooling before complete spreading led to an overestimation by the model; however, it gave a reasonable result that was instructive for explaining the slower cooling for T-BUT versus ACN.

4.4. Influence of solvent system on powder properties

Even though there are substantial differences in the freezing characteristics of each solvent, both solvents produced powders comprising DAN and PVP with similar physico-chemical properties indicating sufficient cooling rates in both solvents. The URF technology was used to manufacture micronized powders containing DAN and PVPK15 in a 1:2 ratio using both ACN and T-BUT as the solvent system.

The rapid freezing of the URF technology produced powders with amorphous characteristics which can enhance dissolution rates through increasing the solubility driving force [35] and lowering the heat of solution of the API [36]. According to the contact angle measurements, wetting of the DAN was improved through the use of the hydrophilic polymer PVP which also acts as a stabilizer to prevent recrystallization of DAN. Even though no statistical difference was seen between the contact angles for the processed powders and the physical mixtures, higher potency powders produced from URF (not published) or SFL [11,14] have shown significant differences in wetting compared to their physical mixture counterparts. Therefore, the decrease in contact angle was attributed to the high amount of PVP included in the composition which masked the increased in wetting attributed to the process. Despite the similar surface areas for both URF micronized powders, the particle morphologies were very different. Both processed powder SEMs revealed discrete nanoparticle domains containing DAN. However, flat plate-like regions were also observed throughout the powder sample in Fig. 6b for T-BUT. This is attributed to a difference in cooling rates between the two solvents [28,29]. The temperature decrease over time at the top of the droplet ($x = 0$) is much slower for the T-BUT droplet which drops 17 K in 600 ms compared to the ACN which drops 75 K within

70 ms. The slower cooling for T-BUT provided time for growth to form the plate-like regions. The growth may have been non-uniform, as more time for growth was available closest to the air surface where the temperature was the highest. However, the freezing rates appeared to be sufficiently fast in both solvents to produce high surface area powders with low crystallinity. Differences in surface morphology could also be attributed to possible differences in solubility within the solvent based on the temperature–composition phase diagram of the API/polymer solution [37,38]. However, these diagrams were not determined and therefore, the extent of this phenomenon on the particle morphology is not known at this time.

5. Conclusions

Sample powders were prepared by URF technology from two different solvents with different thermal and physical properties, T-BUT and ACN. The differences in the thermal properties of the solvent and droplet dimensions had a dramatic effect on the cooling rate of the droplets as evidenced by the heat transfer model and IR studies. An axial heat transfer model for the spread droplets indicated ACN droplets cooled in 72 ms while T-BUT droplets required a much greater time of 483 ms. The much longer cooling time for T-BUT was also observed by FTIR imaging. However, it was found that the rate of cooling was sufficiently rapid in both solvents to produce amorphous powders with high surface areas of the order of 25.9–29.3 m^2/g and high wettability. Relative to physical mixtures, the URF-processed powders had much more rapid dissolution profiles, which were attributed to nano-structured amorphous API domains, and the improved surface areas and wettability. The surface morphology of the powders was different for the two processing solvents, despite the similar surface areas. The primary particles in powders produced from ACN were spherical and uniform in size as a result of the more rapid and uniform cooling of the droplet relative to T-BUT. The use of ACN as a solvent allows for high heat transfer rates, which is beneficial for producing small rapidly dissolving particles, however, its low melting point can cause loss in particle surface area prior to solvent removal. T-BUT, on the other hand, has a lower (but sufficient) heat transfer rate compared to ACN, but is less susceptible to melting at ambient conditions prior to solvent removal. As a result of fast cooling rates and thus high supersaturation, the URF technology is a viable and robust process for producing high surface area nano-structured powders of poorly water-soluble APIs with rapid dissolution rates, which will likely lead to enhanced bioavailability in vivo.

Acknowledgements

The authors kindly acknowledge the financial support from The Dow Chemical Company. This material is based upon work supported in part by the STC Program of the National Science Foundation under Agreement No. CHE-9876674. Kirk A. Overhoff is a continuing American Fellowship for Pharmaceutical Education (AFPE) Fellow from 2004 to 2006 and a 2005–2006 University Continuing Fellowship recipient.

Appendix A. Supplementary data

Supplementary data associated with this article can be found, in the online version, at doi:10.1016/j.ejpb.2006.07.012.8.

References

[1] C. Lipinski, Poor aqueous solubility – an industry wide problem in drug discovery, Am. Pharm. Rev. 5 (2002) 82–85.
[2] A.A. Date, V.B. Patravale, Current strategies for engineering drug nanoparticles, Curr. Opin. Colloid Interface Sci. 9 (2004) 222–235.
[3] R.H. Muller, K. Mader, S. Gohla, Solid lipid nanoparticles (SLN) for controlled drug delivery – a review of the state of the art, Eur. J. Pharm. Biopharm. 50 (2000) 161–177.
[4] K.S. Soppimath, T.M. Aminabhavi, A.R. Kulkarni, W.E. Rudzinski, Biodegradable polymeric nanoparticles as drug delivery devices, J. Control. Release 70 (2001) 1–20.
[5] J.M. Vaughn, R.O. Williams, Nanoparticle engineering, in: J. Swarbrick (Ed.), Encyclopedia of Pharmaceutical Technology, Dekker, in press.
[6] N. Rasenack, B.W. Muller, Micron-size drug particles: common and novel micronization techniques, Pharm. Dev. Technol. 9 (2004) 1–13.
[7] J.H. Hu, K.P. Johnston, R.O. Williams III, Nanoparticle engineering processes for enhancing the dissolution rates of poorly water soluble drugs – a review, Drug Dev. Ind. Pharm. 30 (2004) 247–258.
[8] H. Leuenberger, Spray freeze-drying – the process of choice for low water soluble drugs? J. Nanopart. Res. 4 (2002) 111–119.
[9] Y.F. Maa, P.A. Nguyen, T. Sweeney, S.J. Shire, C.C. Hsu, Protein inhalation powders: spray drying vs spray freeze drying, Pharm. Res. 16 (1999) 249–254.
[10] T.L. Rogers, K.P. Johnston, R.O. Williams, Solution-based particle formation of pharmaceutical powders by supercritical or compressed fluid CO_2 and cryogenic spray-freezing technologies, Drug Dev. Ind. Pharm. 27 (2001) 1003–1015.
[11] J.M. Vaughn, X.X. Gao, M.J. Yacaman, K.P. Johnston, R.O. Williams, Comparison of powder produced by evaporative precipitation into aqueous solution (EPAS) and spray freezing into liquid (SFL) technologies using novel Z-contrast STEM and complimentary techniques, Eur. J. Pharm. Biopharm. 60 (2005) 81–89.
[12] J. Hu, K.P. Johnston, R.O. Williams III, Spray freezing into liquid (SFL) particle engineering technology to enhance dissolution of poorly water soluble drugs: organic solvent versus organic/aqueous co-solvent systems, Eur. J. Pharm. Sci. 20 (2003) 295–303.
[13] T.L. Rogers, K.A. Overhoff, P. Shah, P. Santiago, M.J. Yacaman, K.P. Johnston, R.O. Williams, Micronized powders of a poorly water soluble drug produced by a spray-freezing into liquid-emulsion process, Eur. J. Pharm. Biopharm. 55 (2003) 161–172.
[14] J. Hu, K.P. Johnston, R.O. Williams III, Rapid dissolving high potency danazol powders produced by spray freezing into liquid process, Int. J. Pharm. 271 (2004) 145–154.
[15] J.C. Evans, B.D. Scherzer, C.D. Tocco, G.B. Kupperblatt, J.N. Becker, D.L. Wilson, S.A. Saghir, E.J. Elder, Preparation of nanostructured particles of poorly water soluble drugs via a novel ultra-rapid freezing technology, in: S. Svenson (Ed.), Polymeric Drug Delivery – Polymeric Matrices and Drug Particle Engineering, ACS Symposium Series 924, American Chemical Society, Washington, DC, 2006, pp. 320–328.
[16] N. Ni, M. Tesconi, E.S. Tabibi, S. Gupta, S.H. Yalkowsky, Use of pure *t*-butanol as a solvent for freeze-drying: a case study, Int. J. Pharm. 226 (2001) 39–46.

[17] M.S. Tesconi, K. Sepassi, S.H. Yalkowsky, Freeze-drying above room temperature, J. Pharm. Sci. 88 (1999) 501–506.
[18] S. Brunauer, P.H. Emmett, E. Teller, Adsorption of gases in multimolecular layers, J. Am. Chem. Soc. 60 (1938) 309–319.
[19] J. Fukai, T. Ozaki, H. Asami, O. Miyatake, Numerical simulation of liquid droplet solidification on substrates, J. Chem. Eng. Jpn. 33 (2000) 630–637.
[20] T. Bennett, D. Poulikakos, Splat-quench solidification – estimating the maximum spreading of a droplet impacting a solid-surface, J. Mater. Sci. 28 (1993) 963–970.
[21] B. Kang, Z. Zhao, D. Poulikakos, Solidification of liquid–metal droplets impacting sequentially on a solid-surface, J. Heat Transf. Trans. ASME 116 (1994) 436–445.
[22] J. Madejski, Solidification of droplets on a cold surface, Int. J. Heat Mass Transf. 19 (1976) 1009–1013.
[23] M. Pasandideh-Fard, R. Bhola, S. Chandra, J. Mostaghimi, Deposition of tin droplets on a steel plate : simulations and experiments, Int. J. Heat Mass Transf. 41 (1998) 2929–2945.
[24] M. Pasandideh-Fard, S. Chandra, J. Mostaghimi, A three-dimensional model of droplet impact and solidification, Int. J. Heat Mass Transf. 45 (2002) 2229–2242.
[25] C. Sanmarchi, H. Liu, E.J. Lavernia, R.H. Rangel, A. Sickinger, E. Muehlberger, Numerical-analysis of the deformation and solidification of a single droplet impinging onto a flat substrate, J. Mater. Sci. 28 (1993) 3313–3321.
[26] D. Sivakumar, H. Nishiyama, Numerical analysis on the impact behavior of molten metal droplets using a modified splat-quench solidification model, J. Heat Transf. Trans. ASME 126 (2004) 1014–1022.
[27] G. Trapaga, J. Szekely, Mathematical-modeling of the isothermal impingement of liquid droplets in spraying processes, Metall. Trans. B 22 (1991) 901–914.
[28] G.X. Wang, E.F. Matthys, Modeling of heat-transfer and solidification during splat cooling – effect of splat thickness and splat substrate thermal contact, Int. J. Rapid Solidif. 6 (1991) 141–174.
[29] G.X. Wang, E.F. Matthys, Numerical modeling of phase-change and heat-transfer during rapid solidification processes – use of control volume integrals with element subdivision, Int. J. Heat Mass Transf. 35 (1992) 141–153.
[30] H. Zhang, X.Y. Wang, L.L. Zheng, X.Y. Jiang, Studies of splat morphology and rapid solidification during thermal spraying, Int. J. Heat Mass Transf. 44 (2001) 4579–4592.
[31] Z. Zhao, D. Poulikakos, J. Fukai, Heat transfer and fluid dynamics during the collision of a liquid droplet on a substrate. 2. Experiments, Int. J. Heat Mass Transf. 39 (1996) 2791–2802.
[32] Z. Zhao, D. Poulikakos, J. Fukai, Heat transfer and fluid dynamics during the collision of a liquid droplet on a substrate. 1. Modeling, Int. J. Heat Mass Transf. 39 (1996) 2771–2789.
[33] H.S. Carslaw, J.C. Jaeger, Conduction of Heat in Solids, Oxford University Press, London, 1959.
[34] T. Bennett, D. Poulikakos, heat-transfer aspects of splat-quench solidification – modeling and experiment, J. Mater. Sci. 29 (1994) 2025–2039.
[35] B.C. Hancock, M. Parks, What is the true solubility advantage for amorphous pharmaceuticals? Pharm. Res. 17 (2000) 397–404.
[36] K. Terada, H. Kitano, Y. Yoshihashi, E. Yonemochi, Quantitative correlation between initial dissolution rate and heat of solution of drug, Pharm. Res. 17 (2000) 920–924.
[37] C.Y. Gao, A. Li, L.X. Feng, X.S. Yi, J.C. Shen, Factors controlling surface morphology of porous polystyrene membranes prepared by thermally induced phase separation, Polym. Int. 49 (2000) 323–328.
[38] Y.S. Nam, T.G. Park, Porous biodegradable polymeric scaffolds prepared by thermally induced phase separation, J. Biomed. Mater. Res. 47 (1999) 8–17.